

Protonic surface conduction controlled by space charge of intersecting grain boundaries in porous ceramics

Sindre Ø. Stub, Einar Vøllestad, Truls Norby

Supplementary

1. Methods

1.1 Sample preparation

The starting powder was 8 mol% yttria-stabilized zirconia (8YSZ, TOSOH Corporation, Japan). The surface area of the starting powder was by BET measurements found to be $15.8 \text{ m}^2\text{g}^{-1}$, in agreement with specifications from the producer. The powder was cold-pressed at 100 MPa and sintered at 1000 or 1250°C for 2 h in ambient air. The ramp rate for heating and cooling was $300^\circ\text{C}\cdot\text{h}^{-1}$. The resulting densities of the sintered pellets were 55% (1000°C) and 67% (1250°C) measured by the geometric method (GM). The particle sizes were obtained using ImageJ¹ from SEM images yielding 45 and 250 nm, respectively, for the 1000 and 1250°C samples, hereafter denoted YSZ45nm and YSZ250nm.

1.2 X-ray characterisation and sorption analyses

Phase purity and sample morphology of the pellets were analysed by X-ray diffraction (XRD, Bruker D8 Discover, Cu $K_{\alpha 1}$, Bragg-Brentano) and scanning electron microscopy (SEM, Hitachi SU8200, acceleration voltage of 1 and 15 kV). The BET surface analyses were made using nitrogen physisorption measurements at liquid nitrogen temperature in a relative range of pressure of $0-0.99 p\cdot p_0^{-1}$ (Belsorp-mini instrument, Japan). The samples were outgassed under vacuum overnight at 250°C before the BET measurements. Water adsorption measurements were carried out on 8YSZ-powder (TOSOH Corporation, Japan) and the two samples using water at 25°C (in a relative range of pressure $0-0.99 p\cdot p_0^{-1}$) as feed gas in the physisorption instrument (Belsorp-max instrument, Japan). Before these measurements, the samples were outgassed under vacuum overnight at 400°C.

1.3 Microstructural features of the YSZ samples

Figure S1 shows the XRD diffractograms of the YSZ samples. The N_2 -adsorption isotherms (Figure S2) and pore size distributions (Barrett-Joyner-Halenda (BJH) analyses) (Figure S3) of the BET analyses indicate that there will be marginal contributions from capillary condensation to the amount of water in the samples. Table S1 summarises the microstructural features of the YSZ samples.

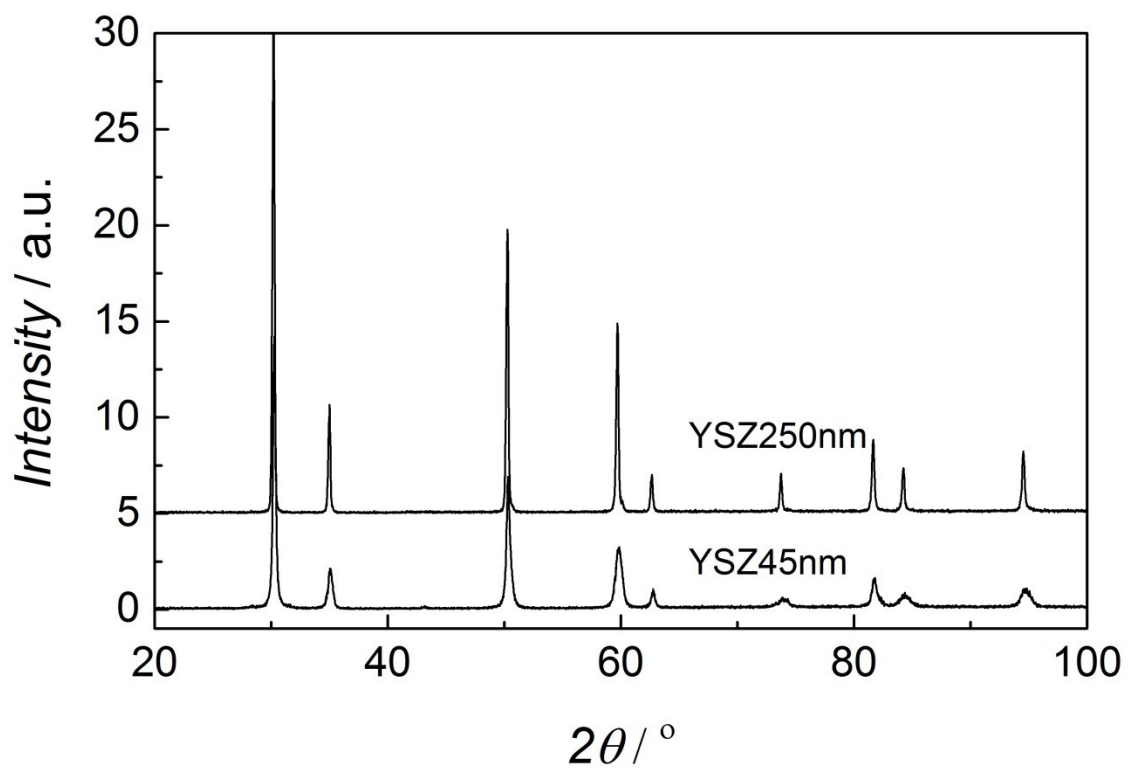


Figure S1. XRD diffractograms of the YSZ samples.

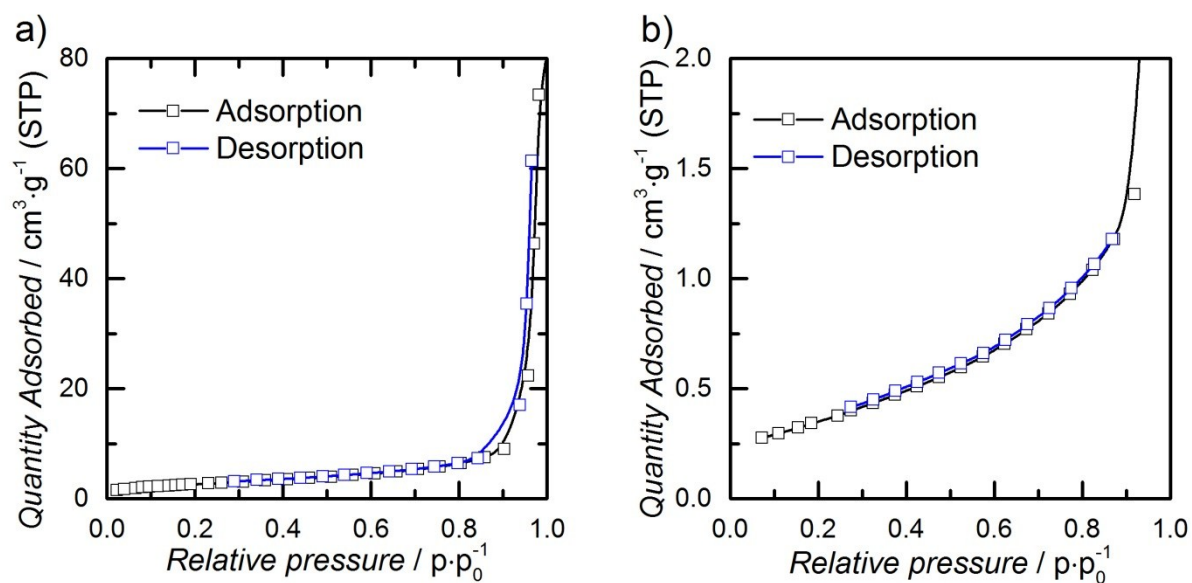


Figure S2. N₂ adsorption isotherms of a) YSZ45nm and b) YSZ250nm.

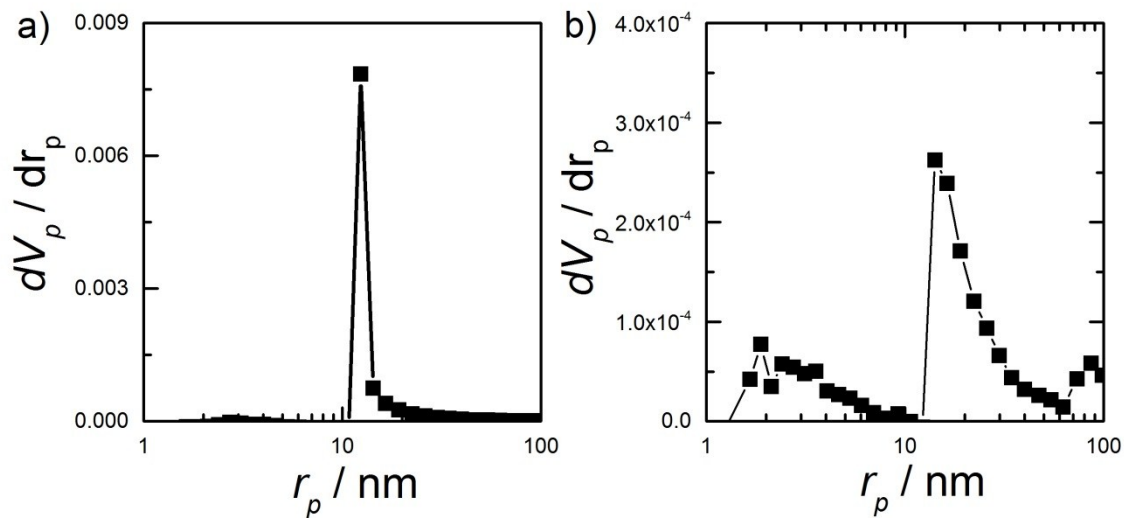


Figure S3. BJH analysis for a) YSZ45nm and b) YSZ250nm.

Table S1 Microstructural features of the YSZ samples.

	YSZ45nm	YSZ250nm
Phases (XRD)	tetragonal and monoclinic	Cubic
Relative density	55%	67%
Particle size (SEM)	45 ± 21 nm	250 ± 75 nm
Crystallite size (XRD)	32 ± 2 nm	-
Surface area (BET)	$9.7 \text{ m}^2\text{g}^{-1}$	$1.3 \text{ m}^2\text{g}^{-1}$
Average pore size (BJH)	49 nm	35 nm

Figure S4 shows the water adsorption isotherms for the samples and YSZ powder corrected for the specific BET surface area of the samples and powder. The uncertainty is assumed to be lower for the powder sample than the actual samples because of higher specific surface area ($15.8 \text{ m}^2\text{g}^{-1}$).

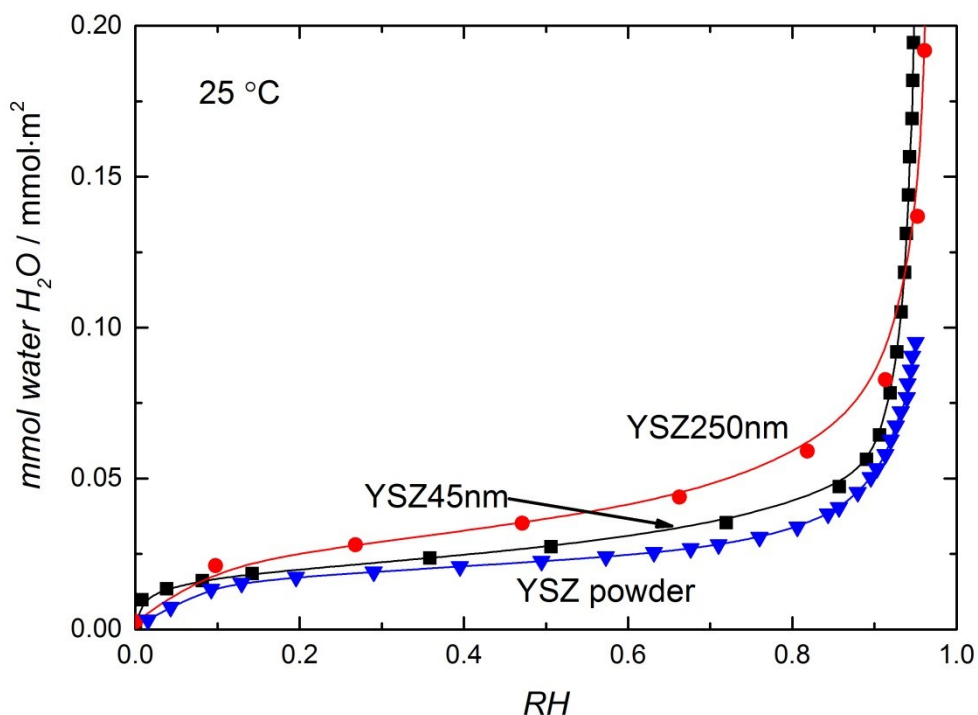


Figure S4. Water adsorption isotherms of the YSZ samples and YSZ powder at 25°C, all corrected for BET specific surface area.

1.4 Electrical measurements and impedance analyses

For the electrical measurements of the sintered pellets, circular Pt electrodes were painted on both sides of the samples using undiluted Pt ink (Metalor UK, Pt ink number 6926). The diameter of the electrodes and the thickness were measured to be 9.30 mm and 0.78 mm for the YSZ45nm sample and 9.90 mm and 0.70 mm for the YSZ250nm sample. The samples with electrodes were annealed at 900°C for 1 h in ambient air to burn off organics residuals in the platinum ink (heating and cooling rates of 300°C·h⁻¹).

Impedance spectroscopy was performed in a ProboStat measurement cell (NorECs, Norway) with a standard 2-electrode 4-wire setup and connected to a Novocontrol alpha-A impedance spectrometer with a ZG4 interface. The impedance spectra were recorded within the frequency range of 10 MHz to 1 mHz, with oscillation voltages in the range 0.1-0.5 V RMS. Specific conductivities for the porous materials were calculated from the macroscopic thickness of the samples and the area of the electrodes. The impedance data were recorded in flowing dry and wet ($p_{H_2O}=0.026$ atm) O₂ as a function of temperature (25-300°C) and at 25°C as function of relative humidity (RH, 0.13-0.84) for the YSZ250nm sample.

Data were analysed and modelled using ZView equivalent circuit fitting software (version 2.9, Scribner Associates Inc.). A parasitic parallel capacitance, C_{stray} , for the empty sample holder was added to the equivalent models presented below before fitting to the measured spectra.

2. Model and procedure for interpretation of impedance spectra

The model used to interpret the impedance spectra corresponds to the paths schematically depicted in Figure S5, with one rail for oxide ion conduction in the grain interior and across grain boundaries, in parallel with another rail for surface protonics over intra-grain surfaces and across inter-grain grain boundaries.

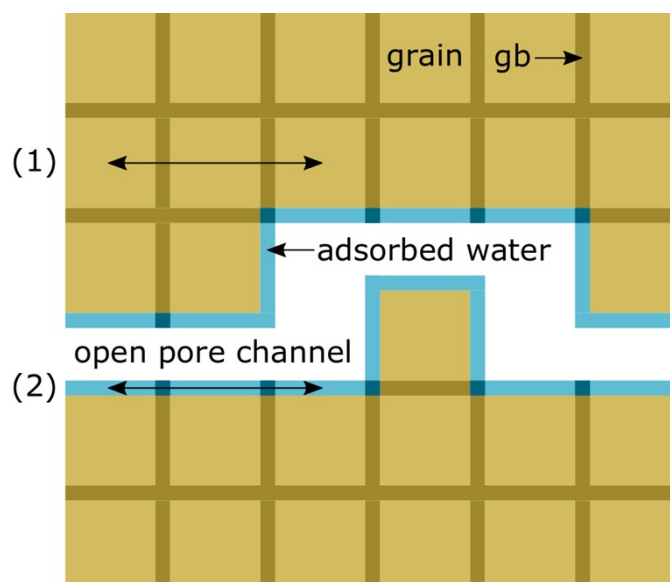


Figure S5: Schematic illustration of the microstructure of a ceramic with open porosity, showing grains, grain boundaries, and pore surfaces. The figure illustrates pathway rails (1) through the grain interior and across grain boundaries (gb), and (2) along the pore surface (intra-grain) and crossing the intersection of the grain boundaries (inter-grain).

Figure S6a-I shows a corresponding equivalent circuit describing the ionic transport and associated capacitances in porous oxides. It comprises the volume transport in grain bulk and across grain boundaries (gb) and surface transport over grain surfaces (intra) and over grain boundary intersects (inter).

YSZ conducts predominantly oxide ions via the vacancy mechanism. The bulk of YSZ does not hydrate significantly, and consequently does not exhibit any significant proton conduction.² The species transported through the grain interior and across grain boundaries are not the same as those transported along surfaces, and the two paths may to a first approximation be treated as separate ionic rails throughout the sample. The contributions from the electrode reactions can be excluded by impedance spectroscopy, and the remaining equivalent circuit then emerges as illustrated in Figure S6a-I.

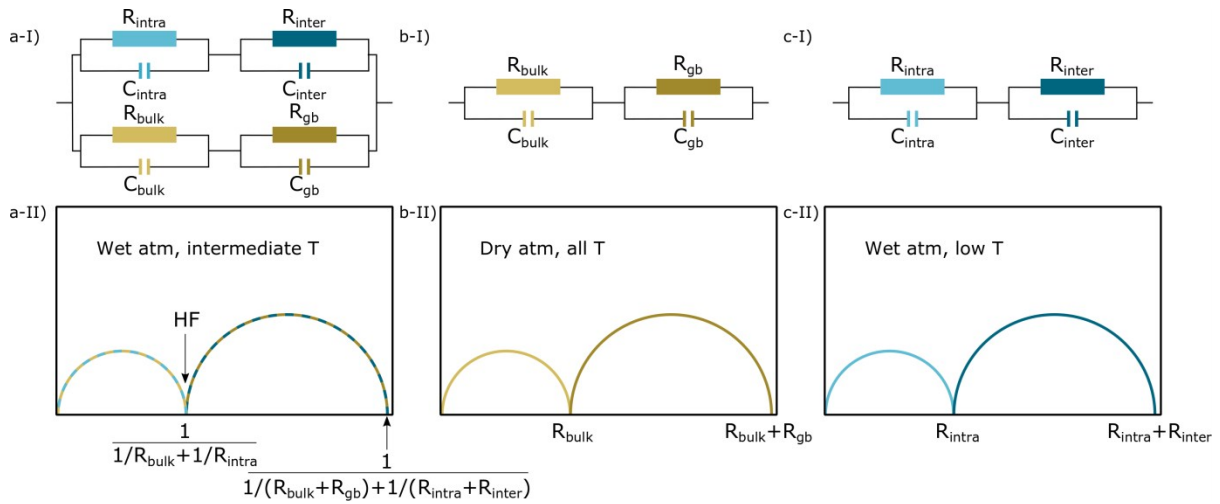


Figure S6: Equivalent circuits (upper) and interpretation of corresponding idealised Nyquits spectra (lower) with related capacitive and resistive contributions for a porous oxide that does not hydrate in bulk, but by adsorption on its surfaces: a) wet atmosphere at intermediate temperatures, b) dry atmosphere and c) wet atmosphere at low temperature. The full circuit for transport through the sample in a-I) shows that the bulk charge carrier is transported through the grain interior (bulk) and across grain boundaries while protonic transport takes place along the surface of the pores (intra-grain) and across the boundary between adjacent grains (inter-grain).

Under normal conditions (typically high temperatures) impedance spectroscopy of polycrystalline ion conducting ceramics yields two distinct arcs in Nyquist plots related to transport through the grain interior (bulk) and across grain boundaries in the material, described by the brick layer model.³ In dry atmosphere, the equivalent circuit in Figure S6a-I can be simplified to the simple series connection through the bulk and across grain boundaries (without the pathway along surfaces). The equivalent circuit and typical Nyquist plot are shown in Figure S6b.

In wet atmosphere, the total impedance of a polycrystalline porous sample will be lowered compared to measuring the same samples under dry conditions, due to the parallel conduction of protonic species along surface of the pores. The full equivalent circuit, as shown in Figure S6a-I, must be used to deconvolute the impedance spectra. In principle, more than two arcs may be observed in the Nyquist plot, but this requires that the RQ elements have significantly different characteristic frequencies, caused by correspondingly different capacitances, while the resistances must be of similar order of magnitude. If the frequencies of the two grain-related processes are similar, and those of the two grain boundary related processes are similar, the plot may end up simplified to only two semicircles, as illustrated in Figure S6a-II.

Data collected in dry atmosphere were deconvoluted without the circuit elements related to surface transport. The data recorded under wet atmosphere were deconvoluted using the full model. The fitting of the measured data in wet atmosphere is done by fixing the resistance and capacitance of interior grain and grain boundary impedances to the values from dry conditions at the respective temperature, whereafter the resistances and capacitances for the surface transport are fitted. At high temperatures, in cases where the inter-grain surface

resistance is negligible under wet conditions, the capacitance associated with grain boundary resistance of oxide ions is allowed to change during the second fitting step.

The total resistance of the porous sample (R_{tot}) is obtained from the series combination of the resistances through the bulk and grain boundaries (R_{bulk} and R_{gb}) and parallel with the series resistance of the resistances of passing over the grain surfaces and grain boundary intersects (R_{intra} and R_{inter}):

$$R_{tot} = \frac{1}{\frac{1}{R_{bulk} + R_{gb}} + \frac{1}{R_{intra} + R_{inter}}} \quad (\text{S1})$$

In wet atmosphere at intermediate temperatures where the surface resistances (R_{intra} and R_{inter}) are comparable to or smaller than the bulk and grain boundary resistances, the surface transport processes will significantly influence the measured impedance. At DC or low frequencies, the entire circuit will take effect. At high frequencies, the higher capacitances of crossing grain boundaries will short R_{gb} and R_{inter} , so that we are left with an intercept in the Nyquist plots corresponding to:

$$R_{HF} = \frac{1}{\frac{1}{R_{bulk}} + \frac{1}{R_{intra}}} \quad (\text{S2})$$

From Equations S1 and S2, it can be seen that the resistance of transport along the pore surfaces, R_{intra} , will affect both of the measured R_{tot} and R_{HF} . The surface grain boundary resistance, R_{inter} , will however only affect the second semicircle. Impedance measurements under dry conditions enable the determination of true bulk and grain boundary resistances. With the R_{bulk} and R_{gb} known, we can determine R_{intra} and R_{inter} from impedance data recorded under wet atmosphere.

At low temperature in wet atmosphere the total conductivity is only related to the surface protonic transport^{4, 5} because $R_{intra} + R_{inter} \ll R_{bulk} + R_{gb}$. The full equivalent circuit in Figure S6a-I can then be simplified to the series processes on the surface, the pure surface transport and the one-dimensional intercepts between the surface and grain boundaries. The equivalent circuit and expected Nyquist plot are shown in Figure S6c.

All in all we see that impedance spectroscopy of porous ionic oxides may produce two arcs in Nyquist plots, but with very different interpretations in the different regimes of temperature and humidity.

3. Electrical characterisation

Examples of Nyquist plots of the two samples at low temperatures are shown in the article Figure 2 and here in Figure S7 for $p_{\text{H}_2\text{O}}=0.026$ atm at 50°C and 75°C, showing for both samples two distinct transport processes in addition to an electrode tail.

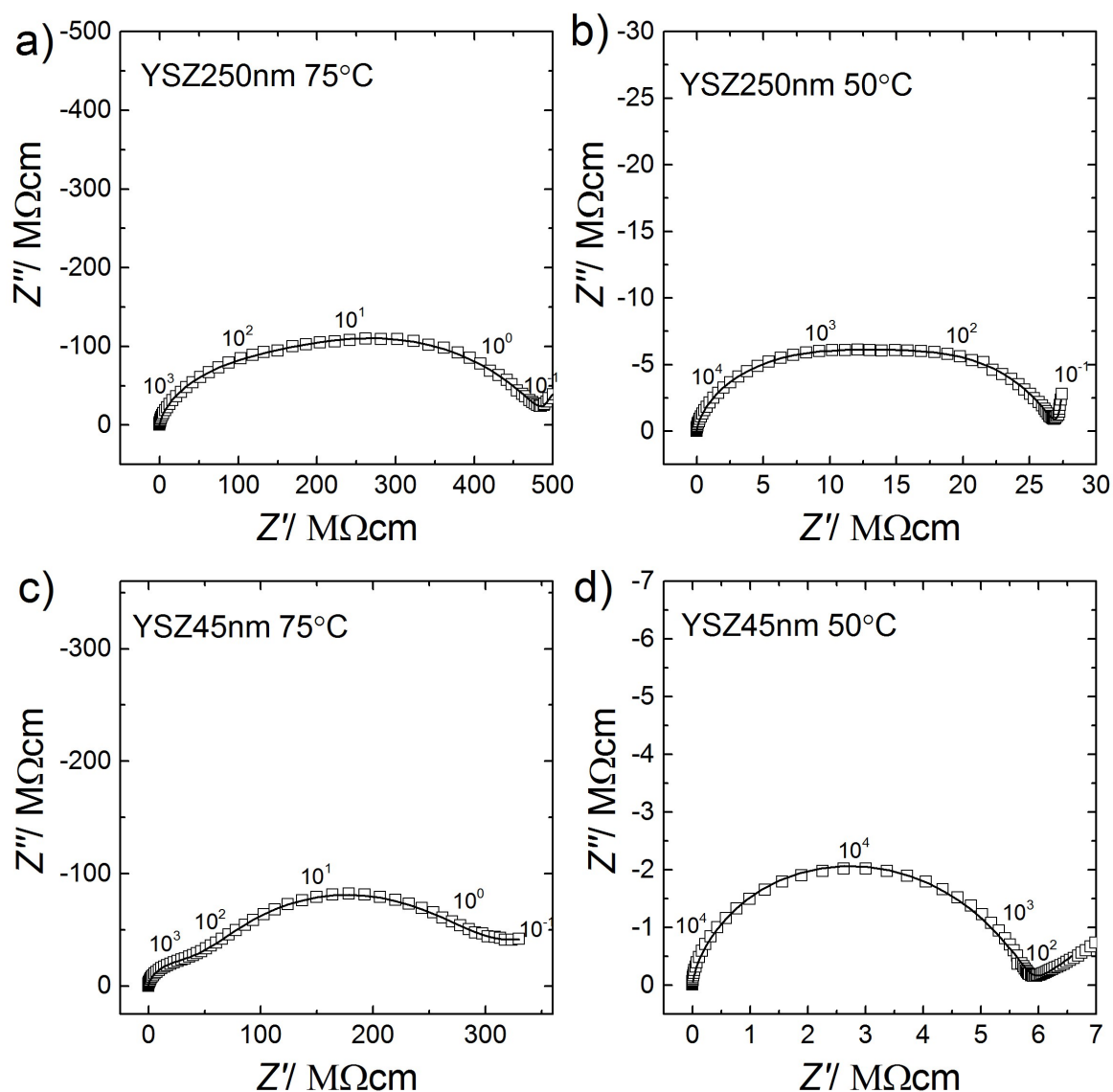


Figure S7 Examples of Nyquist plots under wet conditions ($p_{\text{H}_2\text{O}}=0.026$ atm) for a) YSZ250nm at 75°C, b) YSZ250nm at 50°C, c) YSZ45nm at 75°C, and d) YSZ45nm at 50°C.

Figure S8 shows conductivities and capacitances for the two samples vs $1/T$ from impedance spectra fitted and modelled as described above, corrected with sample macroscopic geometries. The main interpretations are further discussed in the article according to the proposed model. Two further aspects are mentioned here: The C_{intra} for both samples fall unexpectedly at high temperatures. We attribute this to the uncertainty of fitting wet surface protonic parameters at high temperatures using fixed parameters for oxide ion conductivity measured under dry conditions. Moreover, the capacitance C_{gb} associated with the grain

boundary impedance for the 45 nm sample (Figure S8c) is unexpectedly low while C_{inter} appears to vary considerably with temperature (Figure S8c). We attribute this to small grain neck areas of this poorly sintered sample and to a vanishing impedance of the inter-grain process at the lowest temperatures, making the associated capacitances hard to obtain accurately from the impedance spectra. This affects also the accuracy of the delineated resistances under some conditions (see *e.g.* Figure S7d) but the impedance spectra in general leave no doubt of the co-existence of two impedances of comparable orders of magnitude under wet conditions at low temperatures.

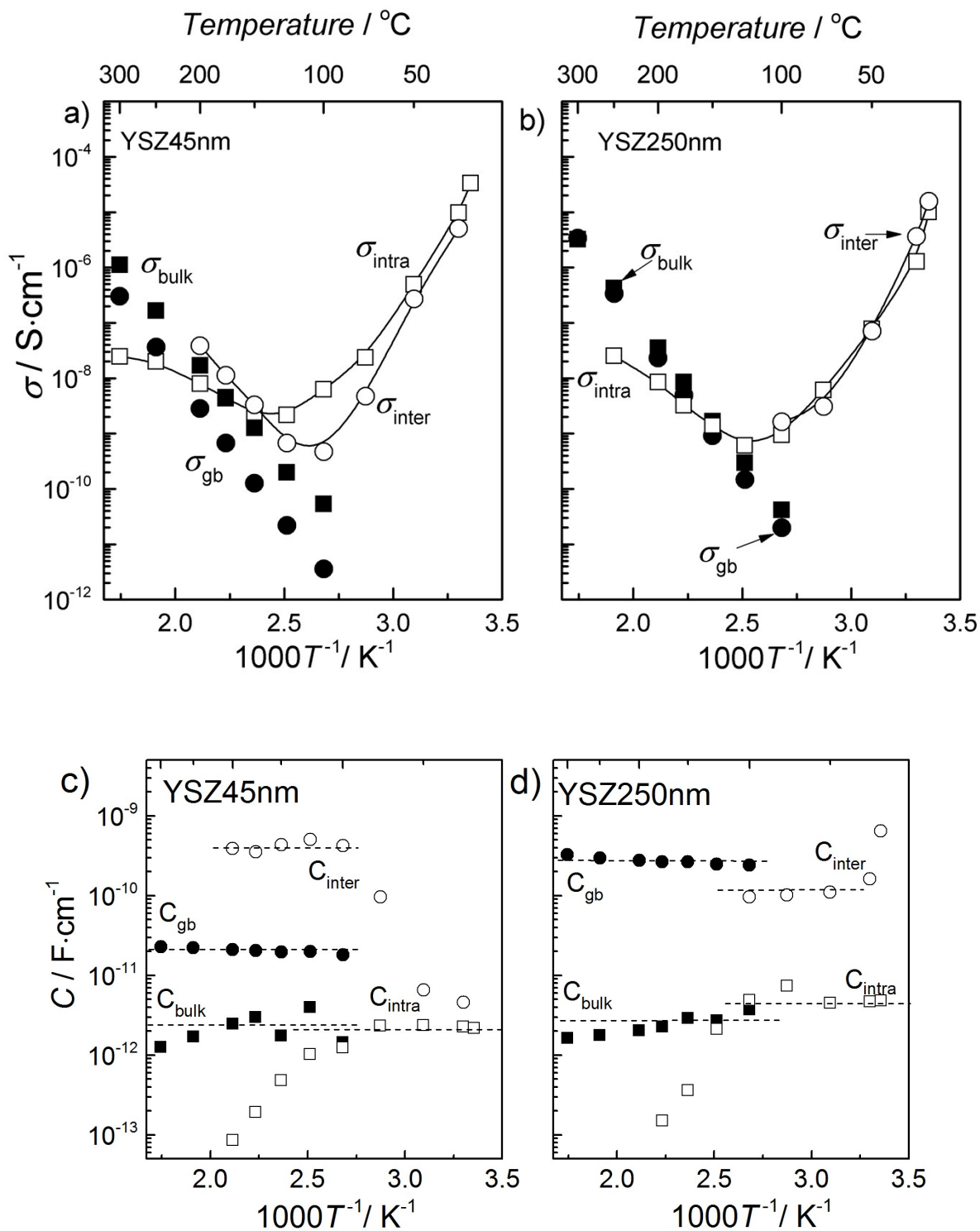


Figure S8. Conductivities and capacitances vs $1/T$ for the YSZ45nm and YSZ250nm samples calculated from the impedance spectra and sample macroscopic geometries. Filled symbols denote oxide ion bulk and grain boundary conduction and open symbols denote protonic surface conduction. Lines are guides to the eye only.

Figure S9 to S15 show Nyquist plots of the YSZ250nm sample at 25°C under various RH (17-84%). Two distinct transport processes in series are observed under all conditions, attributed to intra-grain and inter-grain resistance.

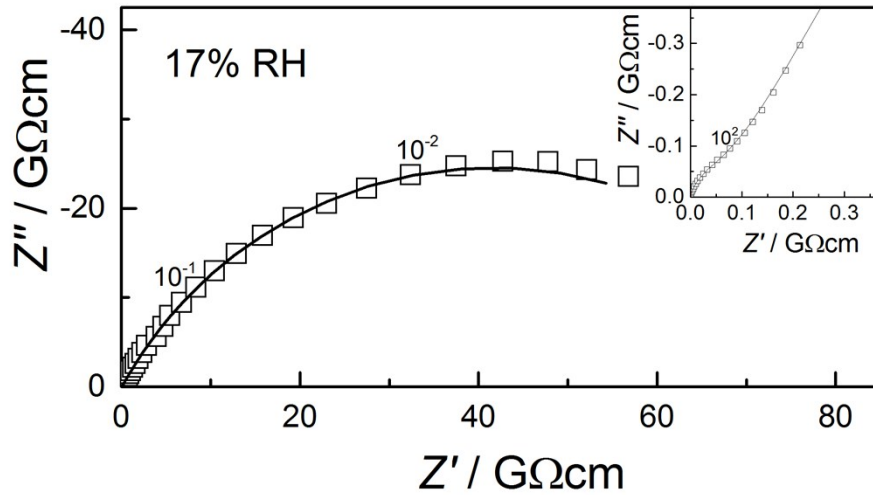


Figure S9. Nyquist plot of YSZ250nm at 25°C and 17% RH.

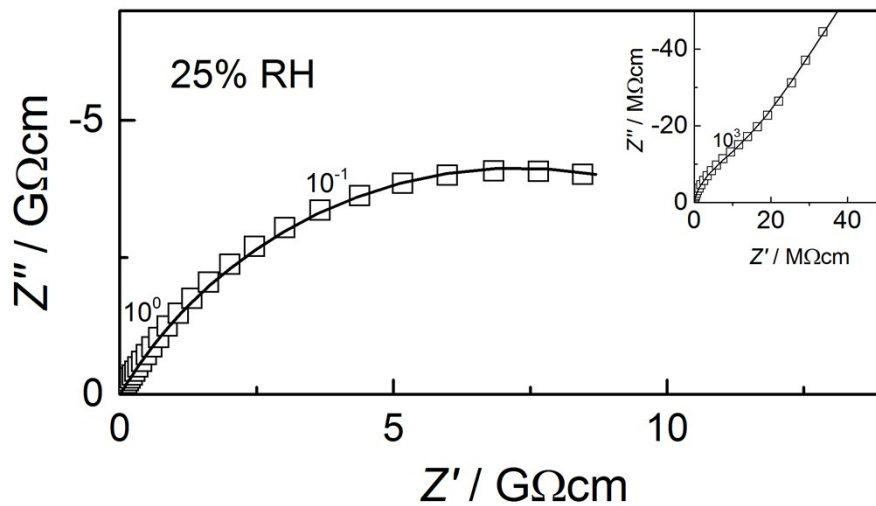


Figure S10. Nyquist plot of YSZ250nm at 25°C and 25% RH.

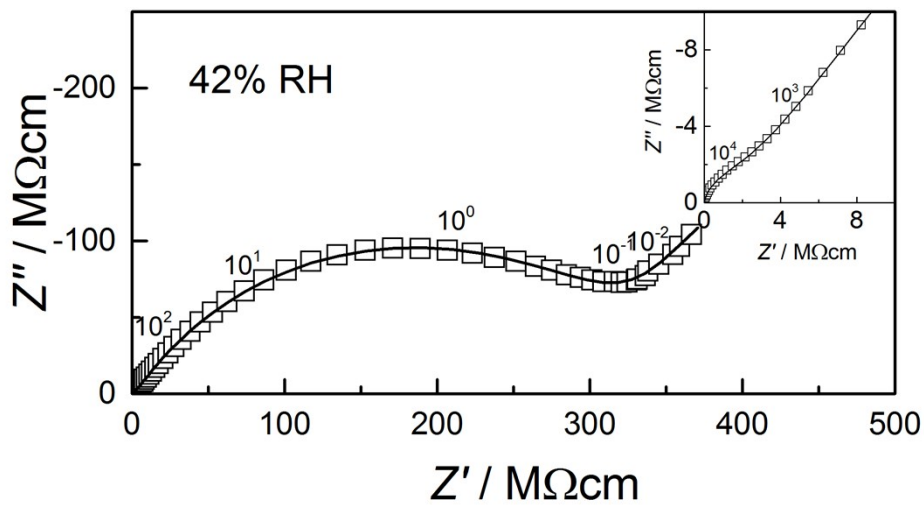


Figure S11. Nyquist plot of YSZ250nm at 25°C and 42% RH.

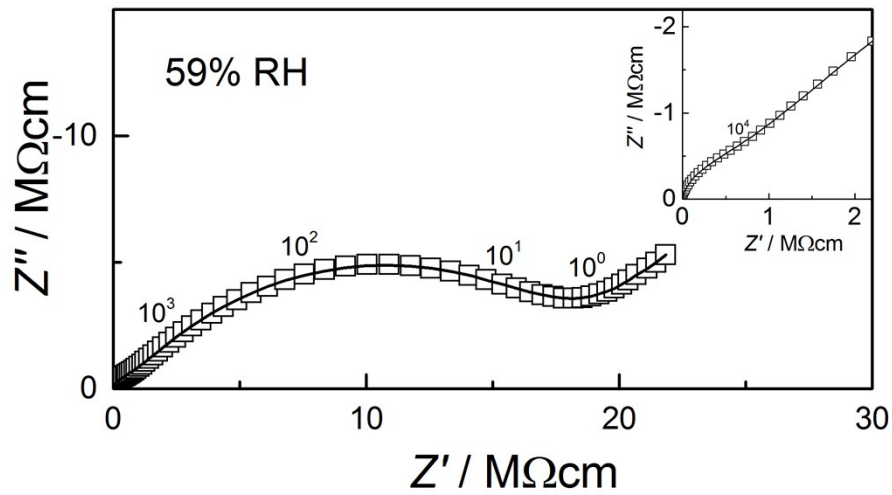


Figure S12. Nyquist plot of YSZ250nm at 25°C and 59% RH.

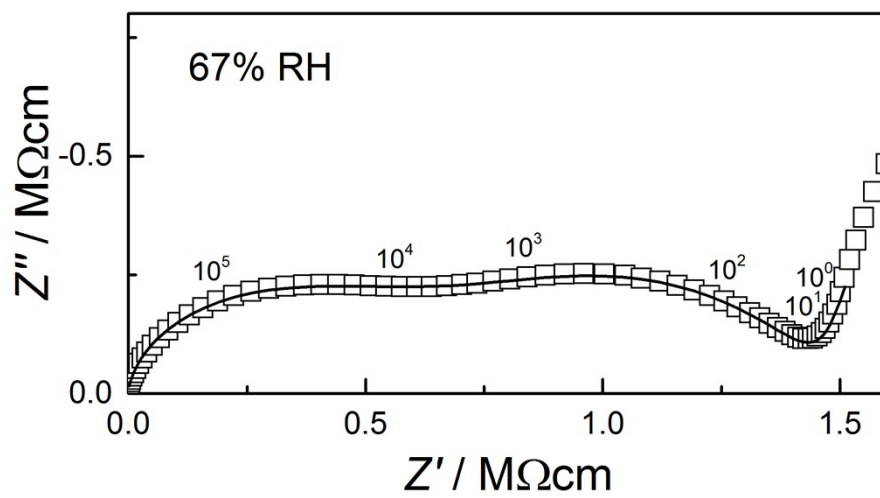


Figure S13. Nyquist plot of YSZ250nm at 25°C and 67% RH.

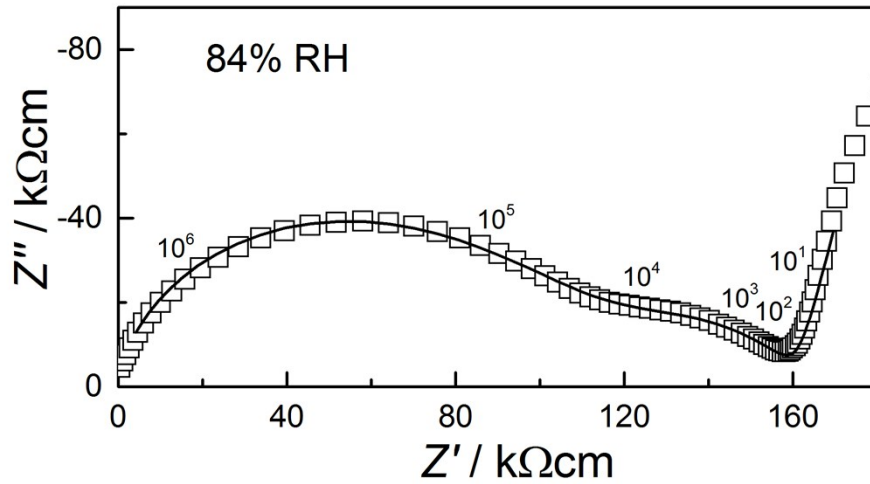


Figure S14. Nyquist plot of YSZ250nm at 25°C and 84% RH.

Figure S15 shows the macro-geometry-corrected capacitances for the intra-grain and inter-grain as a function RH, approximately $3 \cdot 10^{-12} \text{ Fcm}^{-1}$ and $4 \cdot 10^{-10} \text{ Fcm}^{-1}$, respectively, stable within the experimental window.

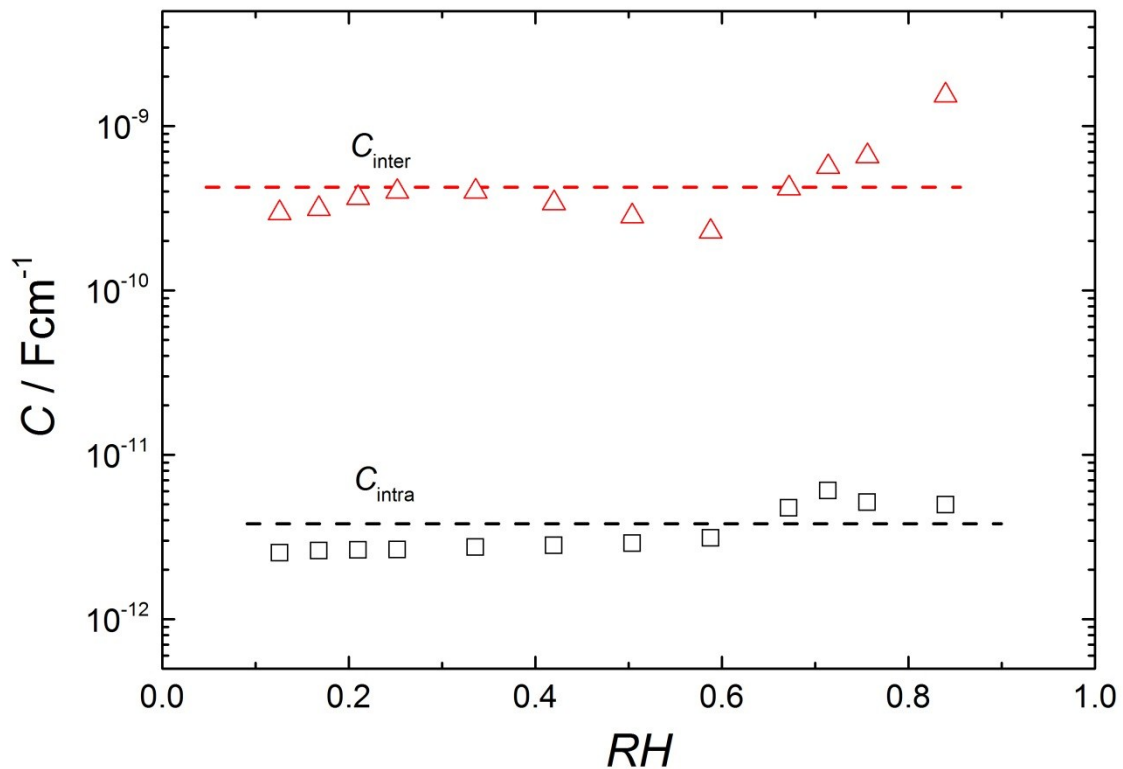


Figure S15. Geometry-corrected capacitances for the YSZ250nm sample at 25°C for intra-grain and inter-grain transport as a function of RH.

Figure S16 shows the apparent specific conductivities of the intra- and inter-grain processes – obtained from impedance spectra for the YSZ250nm sample at 25°C and corrected by the macro-geometry of the sample and electrodes – vs RH.

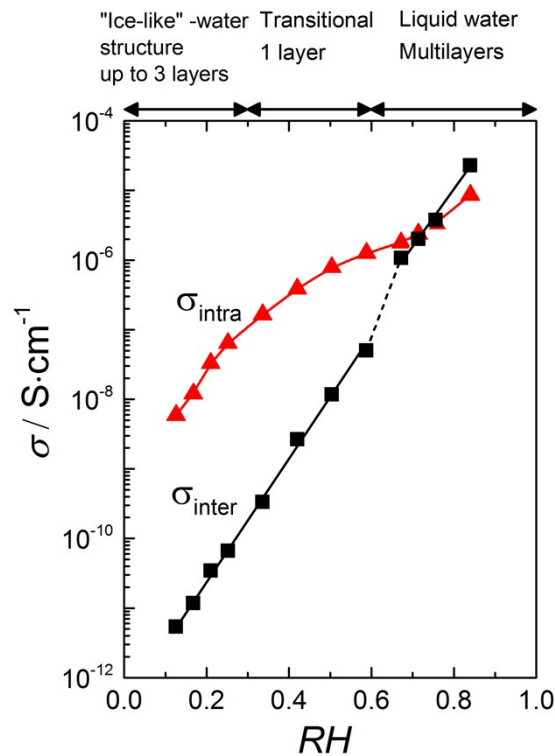


Figure S16: Isothermal conductivities of the 250 nm grained YSZ sample deconvoluted from impedance spectra recorded at 25 °C as a function of RH. The information about the water structure at the top of the figure is taken from Ref.⁶. The lines are guides to the eye only.

4. References

1. Schneider CA, Rasband WS, Eliceiri KW. NIH Image to ImageJ: 25 years of image analysis. *Nat Meth* **9**, 671-675 (2012).
2. Wagner C. Solubility of water vapor in zirconium dioxide-yttrium oxide mixed crystals. *Berichte der Bunsen-Gesellschaft* **72**, 778 (1968).
3. Haile S. The role of microstructure and processing on the proton conducting properties of gadolinium-doped barium cerate. *Journal of materials research* **13**, 1576 (1998).

4. Kim S, *et al.* On the conduction pathway for protons in nanocrystalline yttria-stabilized zirconia. *Physical Chemistry Chemical Physics* **11**, 3035-3038 (2009).
5. Tande C, Perez-Coll D, Mather GC. Surface proton conductivity of dense nanocrystalline YSZ. *Journal of Materials Chemistry* **22**, 11208-11213 (2012).
6. Asay DB, Kim SH. Evolution of the Adsorbed Water Layer Structure on Silicon Oxide at Room Temperature. *The Journal of Physical Chemistry B* **109**, 16760-16763 (2005).